Journal of Hazardous Materials, 33 (1993) 275–293
Elsevier Science Publishers B.V., Amsterdam

Dispersion and deposition of smoke plumes generated in massive fires

Ahmed F. Ghoniem[a], Xiaoming Zhang[a], Omar Knio[a], Howard R. Baum[b] and Renald G. Rehm[b]

[a]*Massachusetts Institute of Technology, Cambridge, MA 02139 (USA)*
[b]*National Institute of Standards and Technology, Gaithersburg, MD 20899 (USA)*

Abstract

Massive fires resulting from the uncontrolled burning of crude oil from spills or industrial accidents produce large smoke-laden buoyant plumes which rise in the wind direction before they equilibrate within a stably stratified atmosphere. Beyond this point, the plume material cools by entrainment and the plume becomes negatively buoyant due to the heavy smoke loading. The trajectory of the descending plume, which determines the ground distribution of smoke, is the subject of this paper. A computational model for the simulation of large-scale smoke plumes resulting from such fires is developed and applied to investigate the effects of the plume initial properties on its trajectory and smoke deposition patterns. Attention is focused on the descent and dispersion of wind-driven plumes in a homogeneous atmosphere, and the smoke deposition on flat terrain. Results show that the plume dynamics in the cross-wind direction are dominated by two buoyantly generated, coherent, streamwise vortices which distort the plume cross section into a kidney-shaped structure. The strength of the two vortices and their separation increase as the plume falls. The plume width grows under the action of these vortices at a rate which increases as the plume settles on the ground, leading to a smoke footprint which does not resemble the prediction of Gaussian dispersion models. The effects of the injection altitude and the initial shape of the plume cross section on the transport and dispersion of the negatively buoyant smoke plume are investigated. Plumes falling from higher elevations disperse more in the vertical direction while those falling from lower elevations disperse further in the horizontal cross-wind direction. Plumes with circular cross-sections reach the ground faster and disperse horizontally further than plumes with elliptical cross-sections with the minor axes in the vertical direction. Vertical plume dispersion is weakly dependent on the shape of its initial cross-section.

1. Introduction

Wind-driven buoyant plumes are responsible for the long-range dispersion of smoke and chemicals emitted from massive fires resulting from oil spills, uncontrolled oil-well fires, and large-scale industrial accidents [1–4]. The

Correspondence to: Ahmed F. Ghoniem, Massachusetts Institute of Technology, 77 Massachusetts Avenue, Room 3-342, Cambridge, MA 02139 (USA). Phone: (617)253-2295, Fax: (617)253-5981, Email address: ghoniem@eddy.mit.edu.

0304-3894/93/$06.00

environmental impact of the fire, which becomes a factor in whether the fire should be fought or left to burn, is determined by the plume trajectory. While the horizontal motion of the plume is governed by the prevailing wind, its vertical motion is determined by buoyancy and is a function of the initial density distribution within the plume cross-section and atmospheric stratification. Typically, the density of the plume* is determined by the temperature and the smoke concentration of the fire plume. Both vary during the plume rise due to entrainment and mixing with the surrounding air. At a certain height, the plume becomes buoyantly stable [5–7] and as it cools further, it starts to fall due to the smoke concentration. Plumes generated by oil fires are of particular interest due to their high smoke loading (10–15 percent of the original fuel burned). The large smoke particulate matter increases the environmental hazard and complicates the analysis, since the smoke cannot be treated as a passive convected scalar. The purpose of this work is to develop a computational model to simulate the buoyant plume dynamics.

Currently available plume models can be divided into two categories [8–12], scale, or integral models; and numerical, or field models. In the former category, dimensional arguments and/or integral conservation expressions are used to derive relations among characteristic, global parameters, such as the maximum plume rise, as a function of the source and ambient conditions. These relationships contain constants, e.g. entrainment rates, which are determined using scaled experiments. In most cases, the plume concentration distribution is assumed to be Gaussian in the plane normal to the plume axis [6, 10]. This simplification limits the applicability of integral models since, as shown below, the underlying assumptions may not hold in many relevant cases. On the other hand, numerical models offer the possibility of more detailed and accurate predictions of the plume dynamics. Typically, these models rely on the numerical integration of the averaged conservation equations, supplemented with turbulence-closure schemes, to describe the field in detail. The application of these models has been limited by the uncertainty associated with the validity of turbulence models in buoyant flows, and the high computational expense associated with using fixed-grid integration schemes.

In this work, a comprehensive numerical model of smoke dispersion and deposition is developed as an effective alternative to both approaches. The model does not rely on experimentally-fitted constants or closure models, and is endowed with efficiency by relying on grid-free, Lagrangian numerical methods to integrate the equations of motion. In this formulation, Lagrangian elements are naturally convected and redistributed in regions of high strain, thereby adapting to severe and rapid changes in the plume structure [13–17]. Far-field and normal boundary conditions are easily applied by using the appropriate form of the Greens function used to represent the velocity induced

* The plume is defined as the mixture of fine combustion products, including smoke particulates, and air entrained and mixed with these products during plume rise.

by a given Lagrangian element. The capability of the model is illustrated by computing the dispersion of a wind-transported dense plume in a uniform atmosphere and its deposition on a flat terrain.

The quantity that is of direct environmental impact is the downwind "footprint" of the smoke plume as a function of fire strength, smoke loading, and wind pattern. This quantity is directly related to the trajectory of the descending plume, a problem which has so far received less attention than rising thermal plumes. Attention is therefore focused on negatively buoyant, descending smoke plumes and their interaction with a flat ground. Much, although not all, of the information required to assess the environmental hazard of the smoke generated from large fires can be obtained from this analysis of the descending smoke plume. We consider cases in which the plume self-induced turbulence far exceed atmospheric turbulence and show that the former plays an important role in determining the plume trajectory and the distribution of smoke within its cross section. We also show that this distribution differs greatly from the conventionally assumed Gaussian due to the formation of strong streamwise vorticity.

The paper is organized as follows. In Section 2, we describe the formulation of the model including the major assumptions used and the non-dimensionalization procedure. The numerical scheme is briefly summarized in Section 3. Detail of the latter can be found in the open literature. In Section 4, results pertaining to the shape of the plume, its trajectory and the smoke distribution are shown and analyzed. The effects of the initial height and shape of the plume are also discussed. Finally, conclusions are presented in Section 5.

2. Formulation of the problem

We consider the evolution of an isothermal smoke plume initially at the thermally stabilized height HT. The plume is characterized by the (excess) particulate mass flux

$$\dot{m}_p = \int \rho_p^* U \, dA,$$

the integration is over the plume cross-wind section, where ρ_p^* is the density of the particulate phase, with the total density $\rho^* = \rho_0^* + \rho_p^*$, and ρ_0^* is the ambient density. The initial plume cross section is taken to be an elliptical cross section of semi-major (horizontal) axis R_y and semi-minor (vertical) axis R_z. The major direction of motion is the horizontal x-direction, with a uniform ambient wind velocity U. The geometry is illustrated in Fig. 1. The specification of initial altitude and shape of the plume cross section is obtained from a plume rise analysis which will be described elsewhere.

The present analysis is based on the following assumptions:

(i) the large-scale plume motion of interest here can be regarded as steady;
(ii) molecular diffusion of mass and momentum are negligible compared with vorticity-induced entrainment;

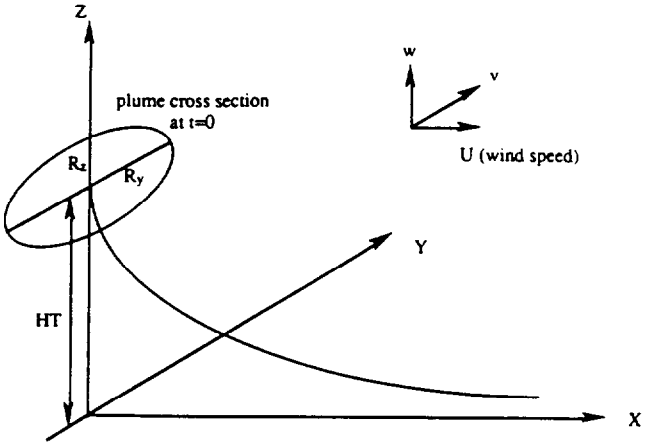

Fig. 1. A schematic representation of the initial plume cross-section and height, its trajectory in the ind direction, the coordinate system and the velocity components.

(iii) the ambient-wind speed U is uniform and much larger than plume-induced velocity components (u, v, w) in the (x, y, z) coordinate directions;
(iv) the smoke particulate can be treated as a continuum fluid;
(v) the stratification and turbulence in the atmosphere can be neglected.

The first four assumptions are quite reasonable and widely adopted in most plume modeling. The last assumption is used as a first-order model for atmospheric conditions. It will be systematically relaxed in future work.

Given the above assumptions, the plume evolution can be described in a transverse (y^*, z^*) plane perpendicular to the ambient wind direction. We introduce dimensionless transverse coordinates, (y, z), and streamwise coordinate, t, as follows:

$$(y, z) = (y^*, z^*)/R_z$$

$$t = \frac{x^*/U}{R_z/V} = \frac{x^*}{U}\sqrt{\frac{\varepsilon g}{R_z}} \tag{1}$$

where $V = \sqrt{\varepsilon R_z g}$, $\varepsilon = \dot{m}_p/\rho_0^* U R_z^2 \ll 1$, and g is the acceleration of gravity. The dependent variables are the transverse velocity components, (v^*, w^*), the perturbation pressure relative to its ambient hydrostatic value, p^*, and the particulate density ρ_p^*. They are made dimensionless as follows:

$$(v, w) = (v^*, w^*)/V$$

$$p = \frac{UR_z}{\dot{m}_p g} p^* \tag{2}$$

$$\rho = \frac{UR_z^2}{\dot{m}_p}\rho_p^* = \frac{\rho_p^*}{\varepsilon\rho_0^*}$$

The conservation of mass, particulates and momentum in the transverse plane then take the form:

$$\frac{\partial v}{\partial y}+\frac{\partial w}{\partial z}=0$$

$$\frac{\partial \rho}{\partial t}+v\frac{\partial \rho}{\partial y}+w\frac{\partial \rho}{\partial z}=0$$

$$(1+\varepsilon\rho)\left(\frac{\partial v}{\partial t}+v\frac{\partial v}{\partial y}+w\frac{\partial v}{\partial z}\right)+\frac{\partial p}{\partial y}=0 \tag{3}$$

$$(1+\varepsilon\rho)\left(\frac{\partial w}{\partial t}+v\frac{\partial w}{\partial y}+w\frac{\partial w}{\partial z}\right)+\rho+\frac{\partial p}{\partial z}=0$$

The quantity ε is a measure of the particulate-to-ambient-air density ratio, proportional to ρ_p^*/ρ_0^*, if ρ_p^* is uniformly distributed over the plume cross-section. This ratio is quite small, typically O(0.01), making the Boussinesq approximation valid in most practical cases. Invoking this approximation, the problem then contains only two non-dimensional parameters, the plume initial stabilization height HT/R_z, and the initial plume aspect ratio $AR=R_y/R_z$. Initially, the particulate density profile within the ellipse must be specified, together with the transverse components of the induced velocity field. In what follows, the initial smoke density is assumed constant, and the transverse velocity components are zero. The velocity components must vanish as $(y, z) \to\infty$, and the normal component of the velocity $w=0$ at the ground $z=0$. For later use in connection with the vortex method, we note that eq. (3) leads to the following evolution equations for the streamwise component of vorticity ω.

$$\frac{\partial \omega}{\partial t}+v\frac{\partial \omega}{\partial y}+w\frac{\partial \omega}{\partial z}+\frac{1}{(1+\varepsilon\rho)^2}\frac{\partial \rho}{\partial y}-\frac{\varepsilon}{(1+\varepsilon\rho)^2}\left[\frac{\partial \rho}{\partial y}\frac{\partial p}{\partial z}-\frac{\partial \rho}{\partial z}\frac{\partial p}{\partial y}\right]=0 \tag{4}$$

where the vorticity is defined as follows:

$$\omega=\frac{\partial w}{\partial y}-\frac{\partial v}{\partial z}$$

The non-Boussinesq terms in the equation are retained mainly for use in future work directed at the near-source plume-rise problem. They play no role in the present problem. Using the vorticity transport equation, the mathematical formulation of the problem is completed by invoking the pressure gradient from the momentum equations,

$$\frac{\partial p}{\partial y}=-(1+\varepsilon\rho)\frac{\mathrm{d}v}{\mathrm{d}t},$$

and,

$$\frac{\partial p}{\partial z}=-\rho-(1+\varepsilon\rho)\frac{\mathrm{d}w}{\mathrm{d}t} \tag{5}$$

and satisfying the conservation of species and incompressibility condition, respectively:

$$\frac{\mathrm{d}\rho}{\mathrm{d}t}=0$$

and

$$\frac{\partial v}{\partial y}+\frac{\partial w}{\partial z}=0 \tag{6}$$

3. Numerical scheme

The vortex element method is used to integrate the vorticity transport equation, eq. (4). The method is based on the discretization of the support of vorticity into vortex elements, and the transport of these elements along particle trajectories. The vorticity of an element is radially distributed in a small neighborhood of its center according to Gaussian core function with a characteristic radius, δ. The velocity field is computed by discrete convolution over the fields of the vortex elements using the desingularized Biot–Savart law. Details of the method, as applied to the plume problem, are described in Refs. [14] and [17]. Vorticity source terms appearing in eq. (4) are evaluated using the transport element method. Similar to the vortex method, the latter relies on the discretization of the density gradient into a finite number of Lagrangian transport elements which move with the local velocity. The density gradient changes with the stretching and tilting of material lines, while the density is obtained by direct summation over the field of transport elements. Details of this method, which has also been applied in combustion problems [15, 16], are given in Ref. [14].

Normal boundary conditions at the ground, $z=0$, are satisfied by accounting for the image system of the vortex/transport elements. We discretize the zone of finite density gradient between the plume and the surrounding using two layers of elements. Both the vortex and transport element methods invoke a redistribution scheme which introduces new elements, as necessary, to maintain the spatial resolution of the computations. This results in an efficient and adaptive solution scheme which captures severe and rapid distortions of the flow map while concentrating the computational effort in zones of finite vorticity and density gradient. The accuracy of this scheme and of the associated plume predictions have been extensively investigated [14, 17].

4. Results

The global structure of descending plumes and of their vorticity field are discussed first for a plume with $HT/R_z=5$, $AR=3$ *and* $\rho=0.106$. The results are

illustrated by plotting, in Figs. 2 and 3, respectively, three-dimensional surfaces of constant smoke concentration and streamwise vorticity. Both figures were obtained by assembling the instantaneous, or local constant smoke density or vorticity contours into a three-dimensional plot, using the computational t-coordinate as a physical x-coordinate. Note that some inevitable numerical diffusion creeps into the plotting procedure, which employs interpolation formulae to find the functional values of smoke concentration and vorticity at the corner of a uniform mesh, that leads to the break-off of some of the plume material into separate blobs. These three-dimensional plots are meant to delineate what a laboratory experiment of a descending plume would show. The results indicate that the initial elliptical plume cross-section is rapidly reshaped into a kidney shaped object and that close to the ground, the smoke distribution is far from the commonly assumed Gaussian.

From extensive computations, and as shown in Figs. 2–4, we find that the large-scale features of the dispersion and deposition of dense plumes can be described in terms of four distinct stages which separate the initial fall and the onset of smoke settlement on the ground. The dynamical processes which distinguish each of these stages are interpreted in terms of the correspondence between the plume structure and the vorticity field, as summarized below. The purpose of devising this way of describing the numerical results is to facilitate

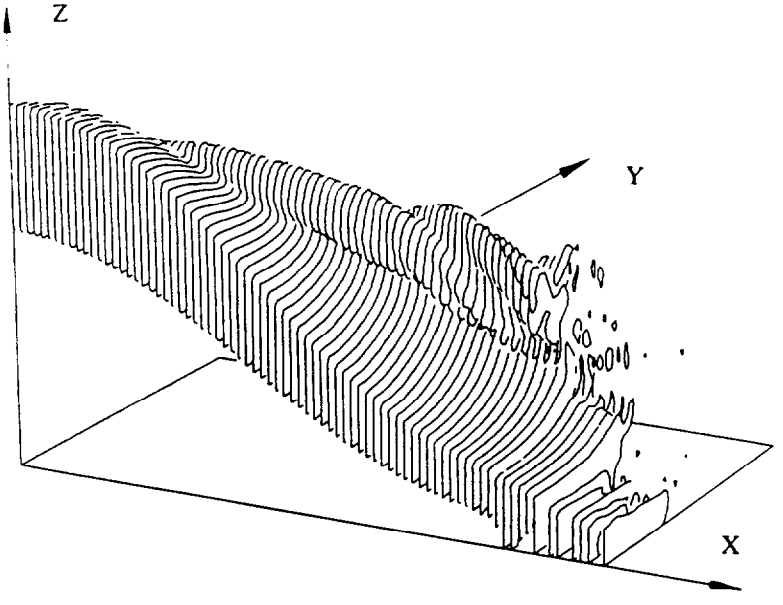

Fig. 2. A three-dimensional perspective plot depicting a surface of constant smoke concentration, $\rho=0.03$, generated for a case with $HT=5R_z$, $R_y=3R_z$, and $\rho=0.106$. Due to symmetry with respect to the x–z plane, contours lying in the $y<0$ region have not been reproduced. The location of the observer is the same as that in Fig. 1.

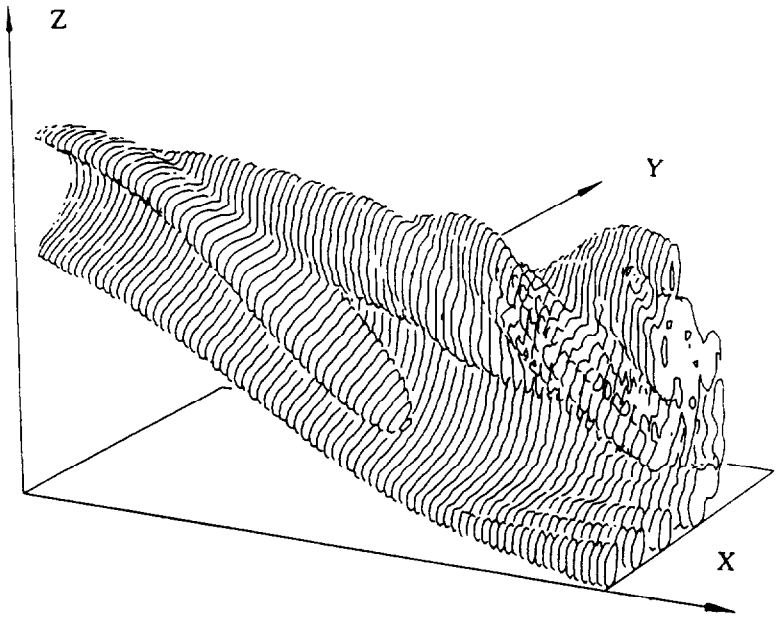

Fig. 3. A three-dimensional perspective plot of streamwise vorticity, $\omega = 0.2$, for the same plume shown in Fig. 2.

their use in formulating future integral models of plume motion. The plume descent starts with an initial acceleration stage, during which the deformation of the plume cross-section is very small and vorticity is generated along the plume air interface. During the second stage, the streamwise vorticity on each side of the plume centerline intensifies and rolls into a large-scale eddy thus generating a counter-rotating vortex structure ($x = 6$–12, in Fig. 4). The induced motion of this vortex pair deforms the plume's smoke distribution into a kidney-shaped cross-section. The structure of the plume at large elevation is in qualitative agreement with the experimental measurements of Hewett et al. [5] who observed a similar kidney-shaped cross-sections downwind the plume source.

With further intensification of the streamwise vorticity under the action of baroclinic torques, small-scale roll-up occurs ($x = 18$–24, in Fig. 4). This third stage is characterized by the generation of streamwise vorticity of opposite signs on both sides of the symmetry plane, and by the increasing complexity of the smoke distribution. Vorticity generation and roll-up transforms some of the plume's potential energy into kinetic energy which is distributed between the plume and its surrounding. The rotational velocity field induced by the vorticity of the plume sets up an entrainment field towards the plume cross-section. Most entrained fluid is engulfed by the large-scale eddy roll-up, while the secondary small eddies induce smaller entrainment currents. The continuous roll-up of the vorticity layer forming on the boundary of the plume cross-section,

which is responsible for maintaining the entrainment towards the plume center, is due to the familiar Kelvin–Helmholtz instability of vorticity layers.

As the smoke approaches the ground, a fourth, ground-settlement stage is observed ($x=24-30$, in Fig. 4). The dynamics of the flow in this stage is increasingly influenced by the proximity to the ground. The associated deceleration field leads to fast and tight widening of the plume structure and its cross-wind straining into two large blobs of smoke connected by a thin crescent. This mechanism is similar to the straining of thermals colliding with walls placed perpendicular to their direction of motion, observed and clearly recorded in laboratory experiments [18, 19]. (Note that mathematically, the behaviour of the plume cross-section in the wind direction is exactly the same as that of a thermal in time.) These experiments show the formation of similar large-scale features and their subsequent separation into two lumps of the thermal fluid as they collide with the wall. The further away from the wall/ground the release point of the thermal/plume is, the more concentrated its material becomes in the two large structures. The early formation of the large-scale features is also depicted by the numerical results of Meng and Thomson [20], who computed the motion of thermals.

One of the important implications of this side roll-up process is the resulting smoke deposition patterns. Clearly, the smoke distribution along the cross section close to the ground is not uniform and may not necessarily possess a maximum at the center $y=0$. This is contrary to classical plume dispersion models which assume that the smoke distribution is Gaussian both in y- and z-directions, and that the smoke ground imprint follows Gaussian function centered at the x-axis of the plume. We note that this departure from a Gaussian distribution is solely due to the plume self-generated vorticity, or turbulence which render the dynamics field surrounding the plume cross-section highly non-uniform.

4.1 The entrainment field

Since most plume models rely on certain assumptions regarding the entrainment field and estimates of the entrainment velocity established by the plume, we examine here, using the numerical simulation results, the form and strength of this field. Besides the formulation of plume models, the entrainment field is used in other applications where the "fire-induced wind" may be important in determining the impact of the fire events on the local environment. Figure 4 shows a superposition of the plume cross-sections and the velocity field in its surrounding for the case shown in Fig. 2. The velocity vectors in the plane of the plume cross-section are displayed as short lines starting from a set of equally distributed mesh points. As indicated above, the roll-up of the vorticity generated along the boundary between the plume material and the surrounding establishes two strong coherent vortices at the far ends of the horizontally expanding plume cross-section. The figure indicates that the field of the large eddy resembles that of a Rankine vortex in which the maximum velocity is reached close to but not at the center of the

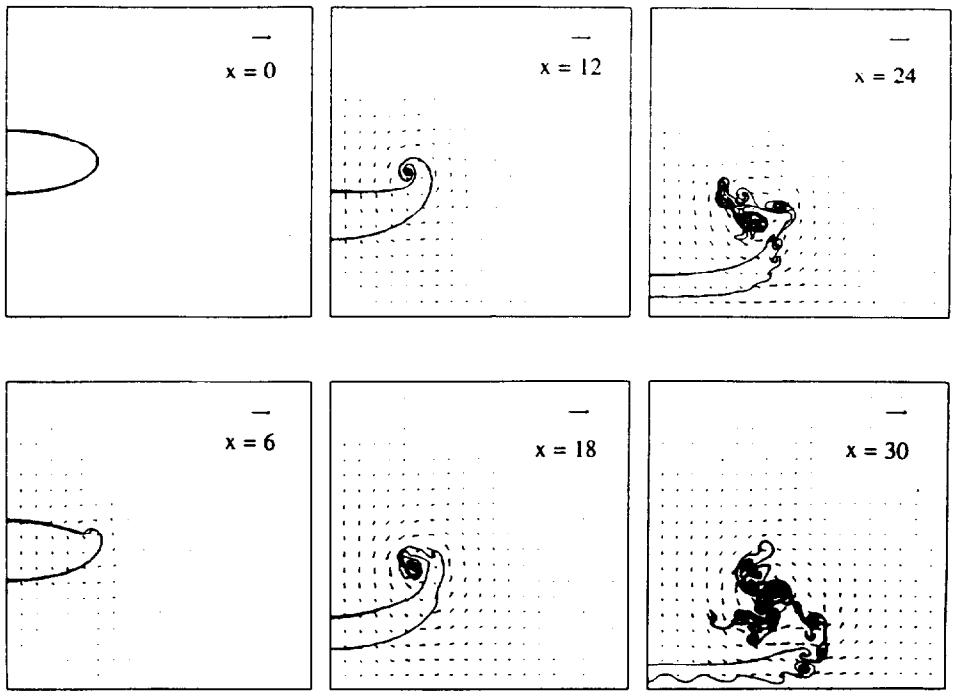

Fig. 4. A superposition of the boundary between the plume and the surrounding, and the velocity induced by the plume motion. The characteristic velocity of the gravity induced flow is shown by the horizontal arrow on the top right-hand corner. The velocity field is shown by a vector whose length is proportional to the velocity, starting from the point where the velocity is computed.

eddy. The maximum entrainment velocity, which as shown in the figure is of the order of magnitude of V, occurs close to the center of the large eddy and stays around the same value for the majority of the plume's journey.

Two interesting observations can be made using these results: The centers of the large eddies stay farther away from the ground than the rest of the plume cross section even as part of the plume material settles on the ground. This means that the turbulent field produced by the plume is not likely to be dissipated quickly as the plume approaches the ground and, at least for some time following the settlement, some circular wind motion will be felt close to the area of plume touch-down. The second observation concerns the waves developing on the lower side of the plume as it touches the ground. The evolution of these waves lead to the formation of small scale eddies which induce their own wind close to the ground, augmenting that induced by the primary large eddies.

4.2 Mechanism of vorticity generation

Detailed flow computations reveal that most of the vorticity generation occurs close to the interface between the plume and the air where density

gradients are high. A short distance away from this interface, the density is uniform, vorticity is zero and the motion is essentially irrotational. A schematic interpretation of the generation and behavior of the streamwise vortices is shown in Fig. 5, where we have invoked the Boussinesq approximation. With $\varepsilon = 0$, the vorticity generation term in the transport equation is proportional to the horizontal density gradient. For a plume with an elliptical initial cross-section, vorticity of opposite signs form on the sides of the plume centerline due to the opposite horizontal density gradients, Fig. 5a, with its maximum absolute value at the far ends. This vorticity layer rolls up to form two large-scale counter-rotating streamwise vortices, so that two additional areas with opposite horizontal density gradients are established on both sides of the plume-air interface, Fig. 5b. Thus, at later stages, vorticity with opposite signs forms on either side of the symmetry plane. The evolution of the vorticity field indicates that a simplified overall plume model which describes the interaction of the plume with its surrounding and its settlement on the ground can be constructed by assuming that the plume dynamics are driven by a kidney-shaped vortex with a time-dependent circulation and width. Values of circulation and distance between the two vortices will be given later.

Extensive numerical experiments have been conducted to investigate the dependence of the results on the initial conditions and plume configurations, the only two parameters left in the problem specification. The dynamics of falling plumes and details of the expected smoke-deposition process are further examined in the following sections. In particular, the effects of initial plume height and shape are discussed in detail. The dependence of the plume width on these two parameters is of special interest since it determines the area contaminated by the plume material. The strength of the plume induced vortex pair is also important since it governs the motion induced by the plume.

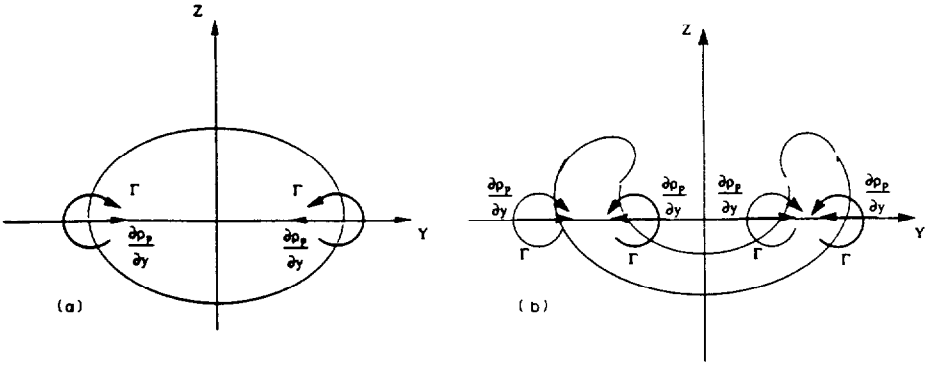

Fig. 5. Schematic illustrations showing (a) the mechanism of baroclinic vorticity generation, and (b) the roll-up of the streamwise vortices and the resulting deformation of the plume cross-section.

4.3 Effect of the initial plume height

Results depicting the plume cross-sections along its trajectory, shown in Fig. 6 for $HT/R_z = 3$ and 30, keeping all other parameters the same, suggest that plumes released from a height close to the ground produce a ground smoke distribution with higher concentration on the sides than at the center. We also find that higher initial elevations lead to more uniform ground-smoke distribution. Moreover, the vertical dispersion is larger for plumes released from higher elevations, while the opposite is true for horizontal plume dispersion. These assertions are illustrated in Figs. 7 and 8 which, respectively, show the

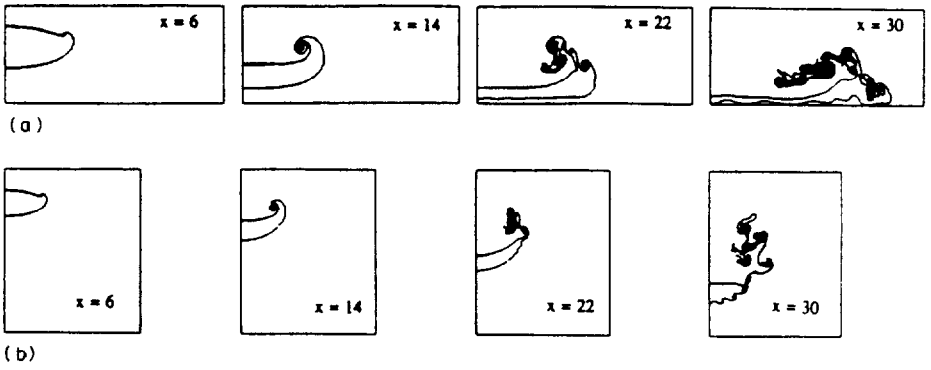

Fig. 6. The plume cross-section at different downwind stations for the case with: (a) $HT/R_z = 3$, and (b) $HT/R_z = 30$. Both cases start with same cross-section and same smoke distribution.

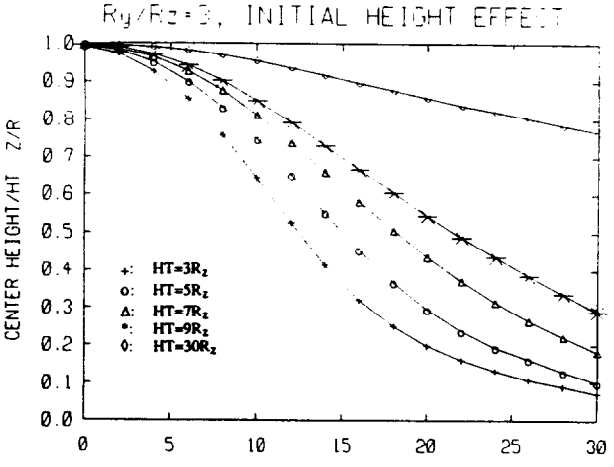

Fig. 7. Streamwise evolution of the height of smoke plumes with $R_y = 3R_z$, and $\rho = 0.106$. Curves are generated for initial heights $HT = 3R_z(+)$, $5R_z$ (○), $7R_z$ (Δ), $9R_z$ (*), and $30R_z$ (◇).

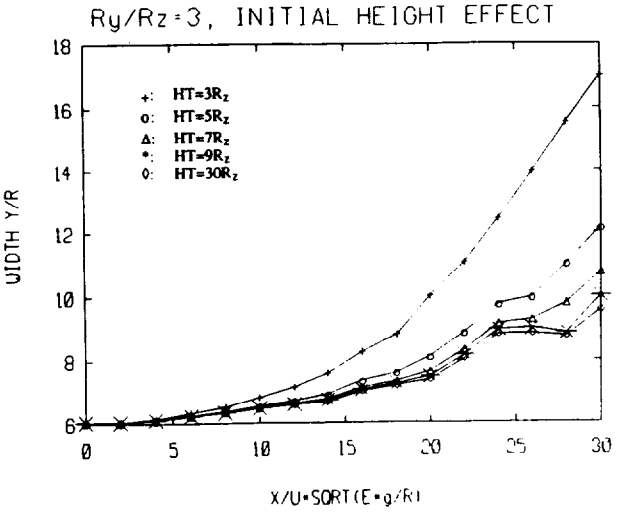

Fig. 8. Streamwise evolution of the width of the smoke plume in Fig. 7. Symbols as in Fig. 7.

trajectories of descending plumes with initial heights in the range $3R_z \leqslant HT \leqslant 30R_z$ and the corresponding horizontal dispersion, defined as the horizontal spread of the plume cross-section.

The plume descent occurs such that most of the horizontal dispersion develops at later stages, when the plume motion is strongly affected by the presence of the ground. When the plume falls from high altitude, its width exhibits an oscillatory behavior. This is due to the intermittent roll-up of large eddies which entrain plume fluid towards their centers as they propagate in the cross-wind direction away from the symmetry plane.

The motion of these large eddies and the generation of smaller scale vortices generate entrainment currents which accompany the horizontal and vertical plume dispersion. The evolution of these currents is measured in terms of the total peripheral length of the interface separating the plume from ambient air at a given cross-section. During the initial acceleration stage, there is little entrainment as the plume suffers a mild deformation. The entrainment rate is higher following large-eddy roll-up which causes the engulfment of a large amount of ambient fluid, and increases further during the later stages when small-scale vortices, generated along the plume surface, induce local entrainment fluxes.

The plume deformation was also correlated with the large-scale features of the baroclinic generation of streamwise vorticity. The latter are determined by the total positive circulation, total negative circulation, and the sum of the two, all computed on one side of the symmetry plane ($y>0$). While the positive circulation, which constitutes most of the vorticity in this region, grows steadily during the early stages, the negative vorticity increases only after large scale roll-up has occurred. Thus, during the first and second stages,

the vorticity field can be modeled as a pair of counter-rotating vortices whose strength increases under the action of the gravitational field. However, at later stages, the single large eddy on each side of the plume should be replaced by a counter-rotating vortex pair, in order to model the generation of both signs of vorticity, and the associated small-scale roll-up and enhanced entrainment rates.

4.4 Effect of initial plume shape

The effect of the initial plume shape on the descent and dispersion processes is now examined. We simulated the motion of plumes with the same cross-sectional area but with different aspect ratios, $AR=1$, 3, 6. In all cases, the initial height $HT=5R$, R being the square root of the initial plume cross-sectional area. Figure 9 shows a comparison between the shape of the plume cross-sections at three cross-sections for $AR=1$ and 6. Figures 10 and 11 show the heights and widths for all three cases, plotted against the downwind coordinate, t, which is defined as the normalized distance travelled from the initial source location.

Examination of these results indicates that different initial cross-sections produce different plume trajectories. This dependency is explained by noting that the rate of vorticity generation, which governs the strength and shape of the large-scale vortices, is strongly dependent on the curvature of the plume boundary. Plumes with small AR, i.e. rounded cross-sections, get more distorted, reach the ground earlier, and disperse horizontally faster than plumes with flatter cross-sections. However, in all cases, the plume tends to break-up into two parts symmetrical about $y=0$. For $AR=1$, this observation is confirmed by experimental results [18, 19]. Moreover, the shape of the initial plume cross-section appears to have a weak effect on the rate of vertical dispersion.

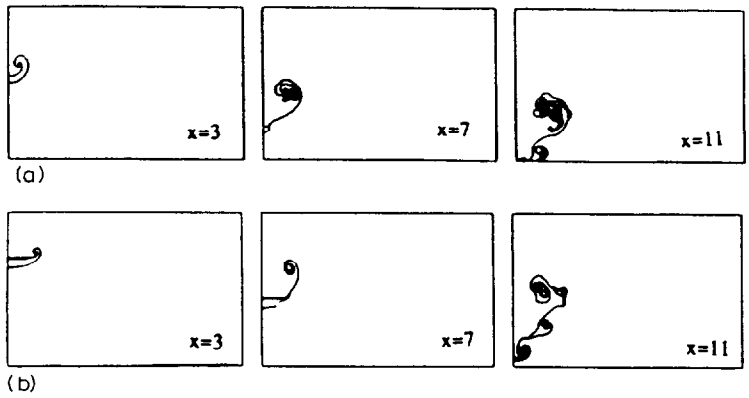

Fig. 9. The plume cross-section at different downwind stations for plumes with: (a) $AR = 1$ and (b) $AR = 6$. Both cases have the same initial height and smoke density distribution within the plume cross-section.

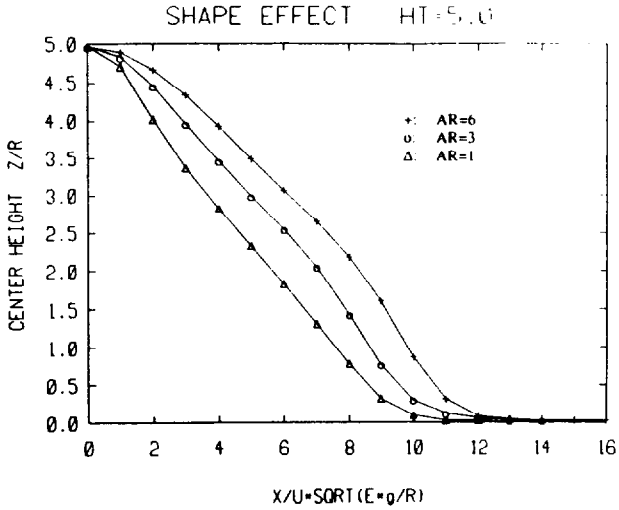

Fig. 10. The streamwise evolution of the height of smoke plumes with $\rho = 1$, $HT = 5R$ and same initial cross-sectional area. Curves are generated for aspect ratios of initial plume sections of $AR = 6$ (+), 3 (○), and 1 (Δ).

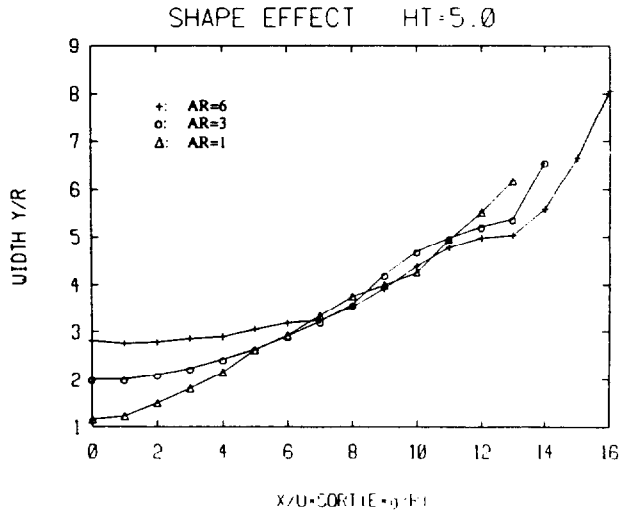

Fig. 11. Streamwise evolution of the width of the plumes in Fig. 10. Symbols as in Fig. 10.

4.5 Global structure parameters

Results presented here, which are supported by other results reported in the literature, show that the motion of the plume, when atmospheric turbulence is weak, is strongly governed by two large streamwise eddies which form due to the roll-up of the vorticity generated along the plume interface. This vortex pair is responsible for the conversion of some of the plume potential energy

into kinetic energy, especially in the plane of its cross section. As we have seen, this kinetic energy is shared by the plume material and the surroundings, and is the source of the strong flow established by the plume motion and the associated entrainment. Thus, it is of interest to characterize this vortex pair by the smallest number of parameters and to study the dependence of these parameters on the initial plume conditions. These characteristic plume parameters could then be used in future plume studies.

A vortex pair can be described by the distance between the centers of the two vortices and the strength of each vortex. The first quantity is proportional to the plume width shown in Figs. 8 and 11. Figure 12 shows the total circulation of each of the vortices for the two cases shown in Figs. 6 and 9, i.e. for different initial plume height and cross section. As expected, vorticity generation, and thus enhancement of the eddies, is fastest during the early stages and is diminished quickly as the plume settles on the ground. The relationship between the acceleration of the plume cross-section, its proximity to the ground and the circulation within its cross-section is shown clearly in Fig. 12b where for a circular plume, which falls the fastest, the circulation rises at the highest slope. Later, and as the plume approaches the ground, the circulation of a circular plume reaches an asymptotic value earlier than any other plume.

5. Conclusions

A novel computational model for the simulation of buoyant plumes has been presented. The model was applied to study the plume dynamics, the dispersion and deposition of its material in a homogeneous atmosphere, and their dependence on the plume initial conditions. Results show that:

(1) Starting from a symmetrical elliptical distribution, the cross-section of descending smoke is deformed into a kidney-shaped structure due to the formation of a counter-rotating streamwise vortex pair. These vortices cause the large-scale engulfment of ambient air towards their centers. At later stages, small-scale vortices develop and enhance entrainment currents.

(2) As the plume approaches the ground, the large-scale eddies acquire a strong cross-wind convective motion away from the symmetry plane. This leads to horizontal dispersion of the smoke plume and results in the deformation of its cross-section into two large lumps separated by a thinning crescent. Accordingly, the ground smoke deposition is lower along the symmetry plane than at neighboring cross-wind locations.

(3) Plume trajectories and dispersion rates are strongly dependent on the initial plume height and shape. The corresponding variations are correlated with streamwise vorticity patterns, whose generation depends on the curvature of the plume interface and on the gravitational acceleration field.

(4) Plumes falling from a higher elevation disperse more in the vertical direction while those falling from a lower elevation disperse more in the horizontal direction.

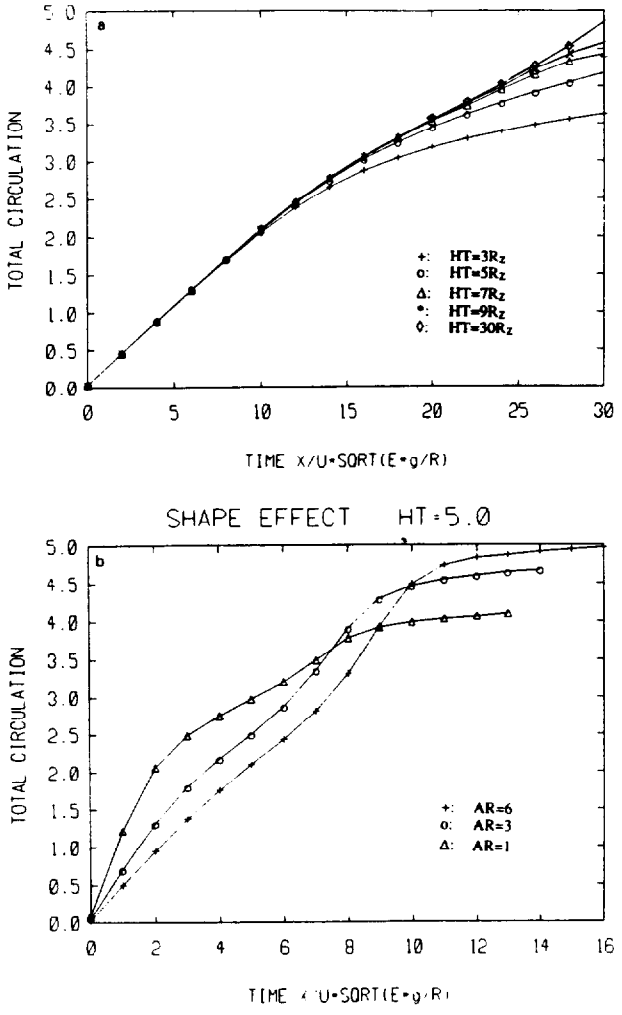

Fig. 12. Variation of the total circulation of each large coherent vortex in the plume cross-section with downwind distance. Shown is the circulation of the right-hand side of the plume for (a) the cases shown in Fig. 7, and (b) the cases shown in Fig. 10.

(5) Plumes with a more rounded cross-section reach the ground faster and disperse horizontally further than plumes with a flatter cross section. The shape of the cross-section has a weak effect on the rate of vertical dispersion.

(6) The strong deformation of the plume cross-section, which leads to a substantial departure of the plume material ground imprint from a Gaussian, is due to the buoyancy generated turbulence within the plume.

Acknowledgement

This work has been jointly supported by the Mineral Management Services of the Department of the Interior and the Building and Fire Research Laboratory of the National Institute of Standards and Technology. We wish to acknowledge Dr. D. Evans of NIST for his review of the paper. The computer, support has partially been provided by the Illinois National Center for Supercomputer Applications.

Nomenclature

AR	$=R_y/R_z$, plume aspect ratio
g	gravitational acceleration
HT	initial height of the plume center
$\dot{m}_p$	$=\int\rho_p^*(y,z)U\mathrm{d}A$, excess mass flux of the plume
p	dimensional perturbation pressure
R	square root of the plume cross sectional area
R_y	major (horizontal) axis of the elliptical plume cross section
R_z	minor (vertical) axis of the elliptical plume cross section
u, v, w	perturbation velocity components in x, y, z direction, respectively
U	uniform wind speed
V	$=\sqrt{\varepsilon R_z g}$, velocity scale of the perturbation velocity
x	horizontal wind direction
y	horizontal direction normal to the wind
z	vertical direction
t	nondimensional form of x^*

Greek

δ	core radius of the vortex and transport element
ε	$=\dot{m}_p/\rho_0^* UR_z^2$, plume mass flux ratio
ρ^*	$=\rho_0^*+\rho_p^*$, total dimensional plume density
ρ_0^*	uniform background air density
ρ_p^*	excess particulate density due to the presence of the smoke
ρ	non-dimensional particulate density
ω	vorticity in the wind direction

Superscript

*	dimensional quantity

References

1 D. Evans, H. Baum, B. McCaffrey, G. Mulholland, M. Harkleroad and W. Manders, Combustion of Oil on Water, Report NBSIR 86-3420, NBS, Gaithersburg, MD, 1986, issued November 1987.

2 D. Evans, G. Mulholland, D. Gross, H. Baum and K. Saito, Environmental Effects of Oil Spill Combustion, Report NISTIR 88-3822, NIST, Gaithersburg, MD, 1987, issued September 1988.
3 D. Evans, G. Mulholland, D. Gross, H. Baum and K. Saito, Generation and dispersal of smoke from oil spill combustion, Proc. of the 1989 Oil Spill Conf. (API/EPA/USCG), February 13–16, 1989, San Antonio, TX.
4 D. Evans, H. Baum, G. Mulholland, N. Bryner and G. Forney, Smoke Plumes from Crude Oil Burns, NISTIR Report, NIST, Gaithersburg, MD, 1992.
5 T.A. Hewett, J.A. Fay and D.P. Hoult, Atmos. Environ., 5 (1971) 767.
6 J.A. Fay, Annu. Rev. Fluid Mech., 5 (1973) 151.
7 W. Rodi (Ed), Turbulent Buoyant Jets and Plumes, Pergamon Press, Oxford, 1982.
8 A. Venkatram and J.C. Wyngaard (Eds), Lectures on Air Pollution Modeling, American Meteorological Society, Boston, MA, 1988.
9 A. Askari, S.J. Bullman, M. Fairweather and F. Swaffield, Combust. Sci. Technol., 73 (1990) 463.
10 J. Seinfeld, Atmospheric Chemistry and Physics of Air Pollution, Wiley, 1986.
11 J.S. Puttock (Ed), Stably Stratified Flow and Dense Gas Dispersion, Clarendon Press, Oxford, 1988.
12 R.E. Britter, Annu. Rev. Fluid Mech., 21 (1989) 317.
13 A.F. Ghoniem, G. Heidarinejad and A. Krishnan, J. Comput. Phys., 79 (1988) 135.
14 A. Krishnan and A.F. Ghoniem, J. Comput. Phys., 99(1) (1992) 1.
15 A.F. Ghoniem, O.M. Knio and A. Krishnan, 23rd Symp. (Int.) on Combustion, The Combustion Institute, London, 1990, p. 699.
16 A.F. Ghoniem and A. Krishnan, 22nd Symp. (Int.) on Combustion, The Combustion Institute, London, 1988, p. 665.
17 A.F. Ghoniem, X. Zhang and O.M. Knio, First Annual Report on Development of a Computational Model for Smoke Plume Dispersion and Deposition, NIST, Gaithersburg, MD 20899, 1992.
18 G. Tsang, Atmos. Environ. 5, 445 (1971).
19 S.J. Barker and S.C. Crow, J. Fluid Mech., 82 (1977) 659.
20 J.C.S. Meng and J.A.L. Thomson, J. Fluid Mech., 84 (1978) 433.